A measure of spatial disorder in particle methods

M. Antuono [a], B. Bouscasse [a], A. Colagrossi [a,*], S. Marrone [a,b]

[a] *CNR-INSEAN, Marine Technology Research Institute, Rome, Italy*
[b] *École Centrale Nantes, LHEEA Lab. (UMR CNRS), Nantes - France*

Abstract

In the present work we describe a numerical algorithm which gives a measure of the disorder in particle distributions in two and three dimensions. This applies to particle methods in general, disregarding the fact they use topological connections between particles or not. The proposed measure of particle disorder is tested on specific configurations obtained through perturbation of a regular lattice. It turns out that the disorder measure may be qualitatively related to the mean absolute value of the perturbation. Finally, some applications of the proposed algorithm are shown by using the Smoothed Particle Hydrodynamics (SPH) method.

Key words: Particle Methods, Meshless Methods, Particle Disorder, Smoothed Particle Hydrodynamics

1 Introduction

In recent years a large amount of studies on particle methods have been developed, these concerning several fields of Physics, Engineering and Mathematics. The increasing interest in particle methods has been driven by their powerful applications and by the attractive mathematical background on which they rely. The main advantage of particle schemes is that they do not implement fixed computational grids but use particles as computational nodes and move them in a Lagrangian fashion. This allows the modeling of complex dynamics with large deformations of the computational domain.

* Corresponding author: *Tel.: +39 06 50 299 343; Fax: +39 06 50 70 619.*
    Email addresses: `matteo.antuono@cnr.it` (M. Antuono),
`benjamin.bouscasse@cnr.it` (B. Bouscasse), `andrea.colagrossi@cnr.it` (A. Colagrossi), `salvatore.marrone@cnr.it` (S. Marrone).

Generally, these schemes may be divided in two wide classes: those which use topological connections between particles (i.e. [1]) and meshless methods (like, for example, [2,3]). For all these schemes, the attainment and maintenance of a regular particle distribution is a crucial point, since the particle disorder may strongly affect their accuracy and stability [4,5]. This challenged many researchers to regularize the particle arrangement through remeshing or shifting algorithms (see, for example, [6–8]). Notwithstanding the idea of particle order/disorder is a natural and innate concept, its theoretical definition and quantitative measurement is hard to identify in a clear and unambiguous manner. This is what we try to address in the present work: we propose a measure of the particle disorder and check it on a number of test cases. These have been gathered in two groups: the former one is made by applications of the disorder measure on different particle distributions while the latter one contains dynamical test cases obtained by using a Smoothed Particle Hydrodynamics (SPH) scheme.

The basic idea for the particle disorder measure relies on the definition of two different *local* distances (that is, distances related to each single particle). The first local distance is simply the minimum distance of a particle from its neighbor particles. The definition of the second local distance is more complex, since this must account for any directional anisotropy in the particle distribution. This may be computed by searching the nearest neighbor particles in different directions and, then, taking the maximum distance all over them.

By construction, the second distance is greater or equal to the first distance. Hence, we define a *local* disorder measure as the ratio between half the difference between the second and the first distance and their arithmetic mean. A *global* disorder measure is obtained as the arithmetic mean of the local measure all over the particles. If the distribution is regular, the first and second distances coincide all over the computational domain, the local measure is zero everywhere and so does the global measure (see Section §2). Then, intuitively, the global measure represents how far the actual particle distribution is from a regular lattice. In Section §2.1 we heuristically found that it has the same order of magnitude of the mean absolute error of the particle distribution with respect to an hypothetical regular distribution. Finally, in Section §3 the global measure has been applied to study dynamical test cases.

2   The particle disorder measure

Let us consider a particle i at the position $\boldsymbol{r}_i$. In particle methods, the i-th particle has its own neighbor particles which may be identified through topological connections (e.g. PFEM) or as particles inside a proper domain
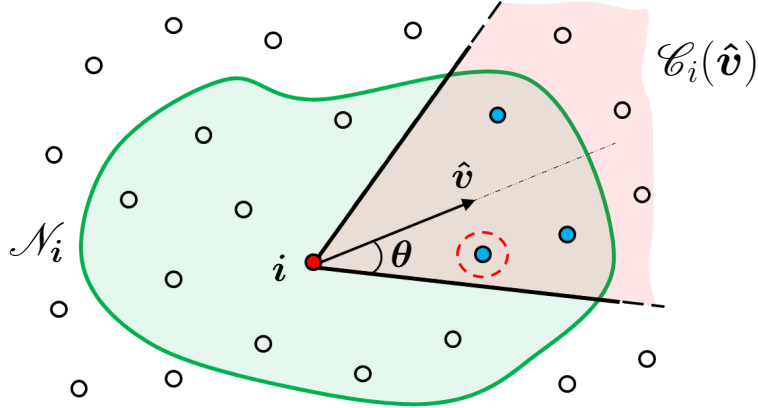
2

Fig. 1. Sketch of a generic set of the neighbor particles, $\mathcal{N}_i$ (green shaded area), and of the cone $\mathscr{C}_i(\hat{\boldsymbol{v}})$ with angle 2θ and axis direction $\hat{\boldsymbol{v}}$ (red shaded area). The selected particle is the nearest to the i-th particle inside the cone.

(as, for example, the compact support of the kernel function in SPH). We denote the set of the neighbor particles to the particle i as $\mathcal{N}_i$ (note that $\mathcal{N}_i$ does not include the i-th particle itself). We define the first local distance as follows:

$$d_m^{(i)} = \min_{j \in \mathcal{N}_i} \| \boldsymbol{r}_j - \boldsymbol{r}_i \| , \tag{1}$$

where $\boldsymbol{r}_j$ is the position of the j-th neighbor particle. If $\mathcal{N}_i$ is empty, $d_m^{(i)}$ is set equal to zero. This is an arbitrary choice and it means that we consider isolated/not-connected particles as a part of disconnected computational domains.

To construct the second local measure, we first define the right circular cone. The vertex of the cone is placed on the i-th particle and its axis is identified by a unit vector $\hat{\boldsymbol{v}}$. The cone aperture is denoted through 2θ. Then, the cone is given by:

$$\mathscr{C}_i(\hat{\boldsymbol{v}}) = \left\{ \boldsymbol{r} \in \mathbb{R}^d \text{ such that } \frac{(\boldsymbol{r} - \boldsymbol{r}_i)}{\| \boldsymbol{r} - \boldsymbol{r}_i \|} \cdot \hat{\boldsymbol{v}} \geq \cos(\theta) \right\} , \tag{2}$$

where d indicates the spatial dimension. A sketch of the cone is displayed in figure 1. The definition of the angle θ is of crucial importance. Specifically, we require that, in the presence of a regular lattice, the cone includes at least one of the nearest neighbor particles (see figure 2). In two dimensions only three regular distributions are possible, namely, the Triangular, the Cartesian and the Hexagonal one. Among these, the Hexagonal distribution has the largest angle between two subsequent nearest particles, i.e. $2\pi/3$ radiants. This suggests that θ has to be larger than $\pi/3$. In three dimensions, the only regular lattice is the Cartesian grid. In this case, we require the cone to be
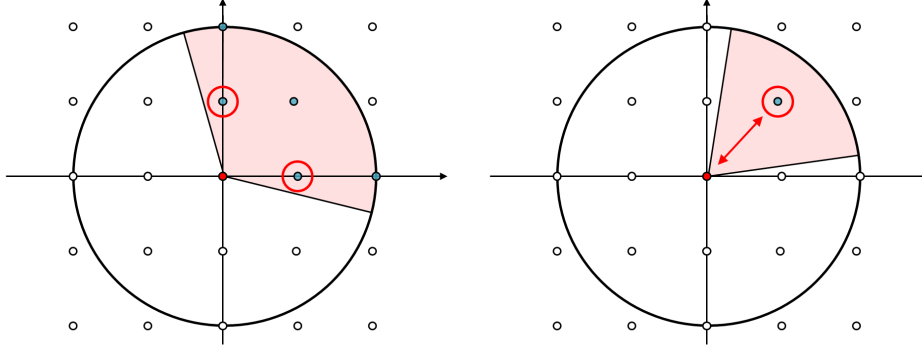
Fig. 2. a sketch with the Cartesian tessellation. Left: a cone with large enough value of θ. Right: a cone with a wrong value of θ.

large enough to include an octant. This corresponds to $\cos(\theta) > 1/\sqrt{3}$ which, similarly to the two dimensional case, approximately corresponds to choosing $\theta \geq \pi/3$. The influence of θ on the results is analyzed in Section §2.1. In all the cases, the axis direction $\hat{\boldsymbol{v}}$ is arbitrary.

After the cone has been defined, we select the neighbor particles inside it and compute the minimum distance from the i-th particle. Then, the cone is rotated (this corresponds to a rotation of the axis or, equivalently, of the vector $\hat{\boldsymbol{v}}$) and the procedure is repeated. In numerical simulations it is not possible to rotate the cone *continuously*. For this reason, we select a finite number of rotations to obtain a cover of the neighborhood of the particle i. This strategy influences the value of the measure we are going to define but it does not alter its global properties. This aspect will be examined in-depth in Section §2.1. For the time being, let us assume that there are k rotations of the cone or, equivalently, k cones with axes identified by unit vectors $\hat{\boldsymbol{v}}_k$. When the neighborhood of the i-th particle has been covered, the second distance is set equal to the supremum of the minimum distances, that is:

$$
d_M^{(i)} = \max_k \left\{ \min_{j \in \mathcal{N}_i \mid \boldsymbol{r}_j \in \mathscr{C}_i(\hat{\boldsymbol{v}}_k)} \|\boldsymbol{r}_j - \boldsymbol{r}_i\| \right\} . \tag{3}
$$

A sketch of the procedure is drawn in figure 3. By construction, this definition allows detecting any eventual anisotropy in the particle distribution and, in case of a regular lattice, it coincides with $d_m^{(i)}$. If any of the k cones is empty (that is, no neighbor particles are inside it), the minimum distance inside it is set equal to zero. This is done to be consistent with the case in which the particle i has no neighbor particle at all. In this way, the above definitions imply $d_M^{(i)} = d_m^{(i)} = 0$.

By construction, the second distance is greater or equal to the first distance. Hence, we define a *local* disorder measure as follows:

4
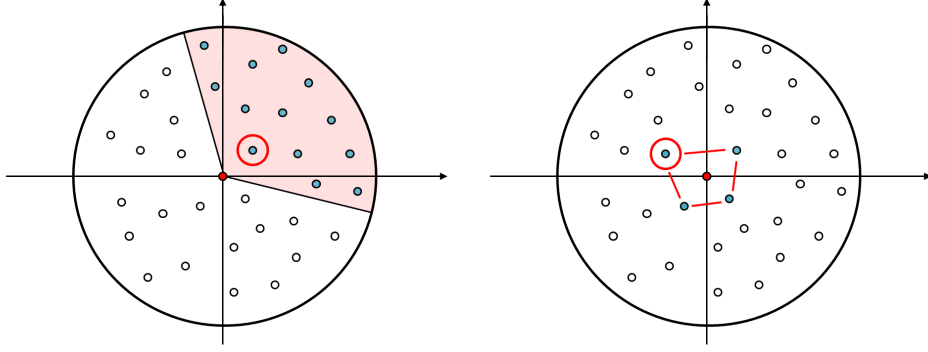
Fig. 3. a sketch of the procedure to build the second distance, $d_M^{(i)}$. Left: the selected particle is the nearest inside the cone. Right: the colored particles are the nearest in each cone. The farthest among them gives $d_M^{(i)}$.

$$\lambda_i = \begin{cases} \dfrac{d_M^{(i)} - d_m^{(i)}}{d_M^{(i)} + d_m^{(i)}} & \text{if} \quad d_M^{(i)} > 0 \,, \\[2em] 0 & \text{if} \quad d_M^{(i)} = 0 \,. \end{cases} \tag{4}$$

The latter case corresponds to isolated particles. Obviously, we exclude from the present analysis the eventuality that all (or a great part of) the particles are isolated. Finally, the global measure of the particle disorder is defined as follows:

$$\Lambda = \frac{\sum_i \lambda_i}{N} \,, \tag{5}$$

where the summation is performed over all particles and N is the total number of particles. Since $\lambda_i \leq 1$, it is $\Lambda \leq 1$ as well. If the particle distribution is regular, the second and first local distances coincide all over the computational domain. Consequently, λ_i is zero everywhere and $\Lambda = 0$. This means that we can use Λ as a qualitative measure which indicates how far the actual particle distribution is from a regular lattice. In the next section, we show that Λ has the same order of magnitude of the mean absolute error of the particle distribution with respect to an hypothetical regular distribution.

Before proceeding to the analysis, we would like to stress a further point. No hypothesis has been done on the set of neighbor particles, meaning that the measure Λ is well posed whatever the form of $\mathcal{N}_i$. Specifically, the definition of $\mathcal{N}_i$ only depends on the numerical scheme under consideration.

2.1 Tests on irregular particle distributions

In this section we use Λ to measure the disorder on irregular particle distributions. These have been obtained by superimposing a random noise (Gaussian or Uniform) on regular distributions (Hexagonal, Cartesian and Triangular in two dimensions and Cartesian in three dimensions) characterized by a mean particle distance equal to Δx. The random noise has zero mean and mean absolute value equal to $\epsilon_r \Delta x$. Specifically:

$$\epsilon_r \,=\, \frac{1}{N} \sum_i \frac{\|\boldsymbol{r}_i - \hat{\boldsymbol{r}}_i\|}{\Delta x}\,, \tag{6}$$

where $\hat{\boldsymbol{r}}_i$ indicates the particle position on the regular grid. This parameter represents the mean absolute relative error with respect to the regular grid. As shown in the sequel, ϵ_r can be easily correlated with the measure of disorder and, therefore, it is preferred to a characterization based on the variance of the random noise (as done, for example, in Vacondio et al. [9]). Incidentally, we observe that the variance is not constant but depends on ϵ_r because of the assignment on this parameter. This is explained in details in appendix A. The results shown in the sequel have been obtained by using a squared domain with about 6400 particles (the number of particles slightly varies according to the tessellation under consideration).

The analysis of the measure Λ is made by varying the angle θ and the number of cones (see Section §2). As explained in the previous section, the directions of the cone axes are completely arbitrary since we just need to cover the neighborhood of the i-th particle. In any case, we prefer to give a recipe to set these directions in a simple and reliable way. Let us consider k cones centered on the i-th particle. The axis of the first cone is defined by using the direction given by the i-th particle and its closest neighbor particle. In two dimensions the remaining $(k-1)$ directions are selected by dividing the two-dimensional space in k identical sectors. For what concerns the three dimensional space, the possibility of choosing the remaining directions in a "regular" way is limited to few specific cases. For example, the axis directions may be chosen as the vertexes of regular polyhedra centered on the i-th particle. This leads to $k = 4, 6, 8, 12, 20$ according to the adopted polyhedron (e.g., tetrahedron, octahedron, cube, icosahedron or dodecahedron).

The first three plots of figure 4 display the behavior of the measure Λ applied to two-dimensional regular grids perturbed by a Gaussian noise ($\epsilon_r = 0.1$). The error bars represent the variance of the *local* measure λ_i. We vary both the number of cones and the angle θ. In all the cases the increase of the number of cones generally corresponds to a slight increase of Λ even if the discrepancies rapidly decrease as the angle becomes larger and larger. Specifically, for values
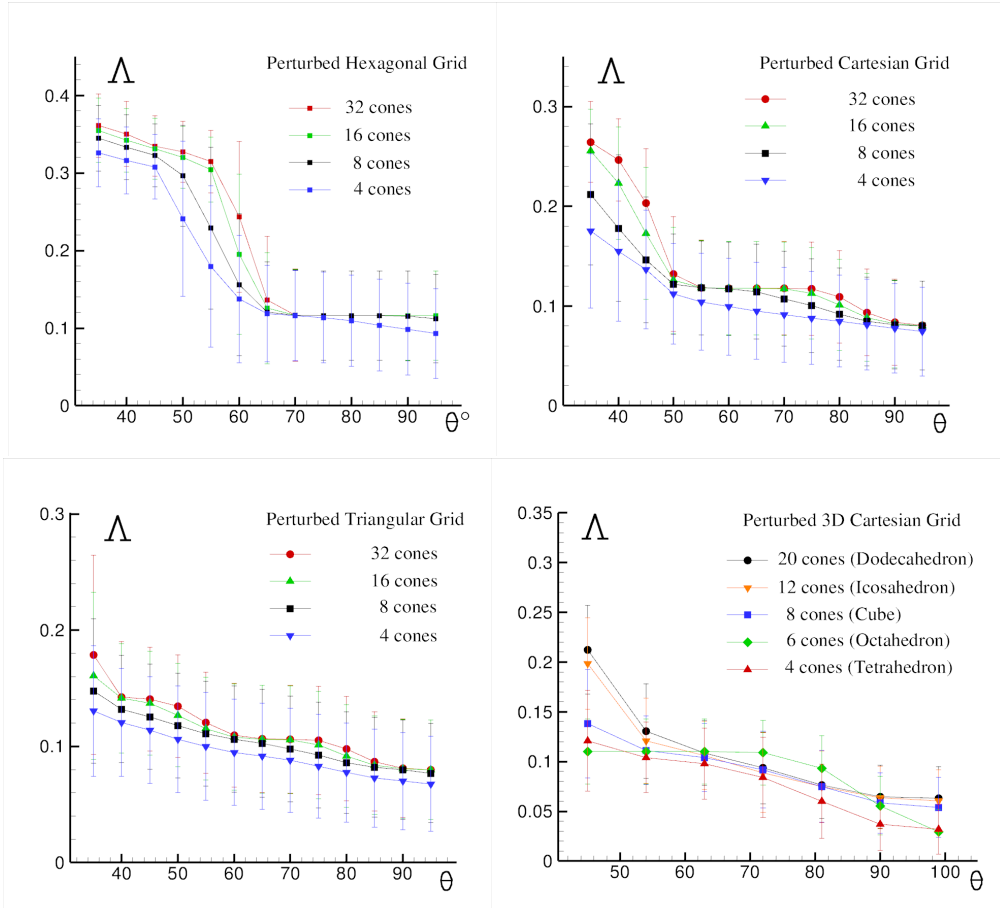
6

Fig. 4. The measure Λ applied to two-dimensional regular grids and to a Cartesian three dimensional grid perturbed by a Gaussian noise ($\epsilon_r = 0.1$). The angle θ is measured in degrees.

of θ that are sufficiently large, the measure Λ seems to approach a plateau. This "asymptotic" value of Λ has an order of magnitude which is comparable to the error ϵ_r (plotted as the abscissa) and this means that Λ may be used as a qualitative measure for the particle disorder. Similar behavior has been observed in three dimensions (see the bottom right panel of figure 4). These results maintain almost identical by using a Uniform noise instead of a Gaussian noise. Incidentally, we recall that Λ is well posed only for $\theta > \pi/3$ (see previous section) and this motivates the large discrepancies observed in figure 4 when $\theta < \pi/3$.

The above analysis suggests that it is not necessary to use a large number of cones but it is preferable (and computationally more convenient) to use few cones with a large enough angle. Then, in both two and three dimensions we choose 8 cones and $\theta = 7\pi/18$ (that is, $\theta = 70°$). Some examples of the behavior of the measure Λ with $\theta = 7\pi/18$ are drawn in figure 5 as function of the noise ϵ_r. These plots confirm that Λ is comparable to ϵ_r and that the measure is only slightly influenced by the increase of the number of cones.
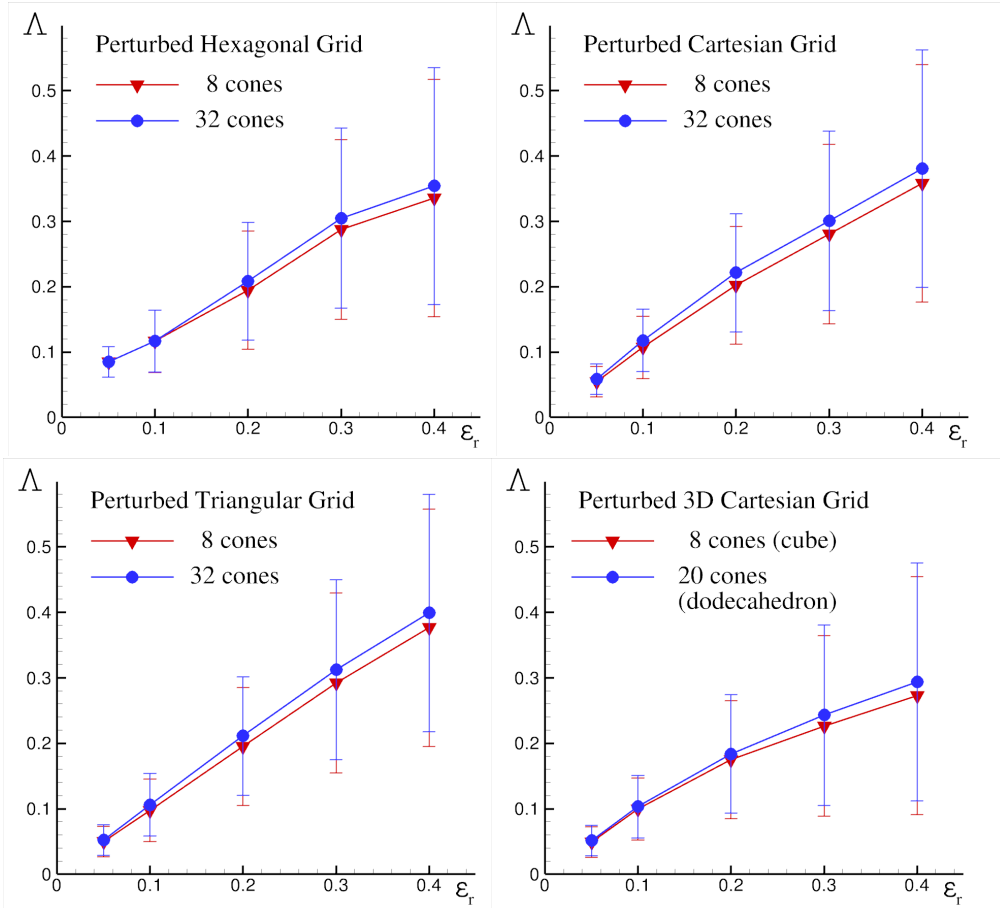
7

Fig. 5. The measure Λ with $\theta = 70°$ applied to two-dimensional regular grids and to a Cartesian three dimensional grid perturbed by a Gaussian noise.

3   Applications

In the following sections we show some useful applications of the proposed measure of spatial disorder. We use the Smoothed Particle Hydrodynamics scheme (SPH hereinafter) since this is one of the most widespread particle methods in the fluid-dynamics community. In its standard form, the SPH scheme relies on the assumption that the fluid is weakly-compressible and barotropic. Specifically, the SPH equations read:

$$\begin{cases} \dfrac{D\rho_i}{Dt} = -\,\rho_i \sum_j (\boldsymbol{u}_j - \boldsymbol{u}_i) \cdot \nabla_i W_{ij}\, V_j \\[4mm] \dfrac{D\boldsymbol{u}_i}{Dt} = -\,\dfrac{1}{\rho_i} \sum_j (p_j + p_i)\, \nabla_i W_{ij}\, V_j + \boldsymbol{f}_i + \dfrac{\mu}{\rho_i} \sum_j \pi_{ij}\, \nabla_i W_{ij}\, V_j \\[4mm] \dfrac{D\boldsymbol{r}_i}{Dt} = \boldsymbol{u}_i \qquad\quad p_i = c_0^2\,(\rho_i - \rho_0) \end{cases} \qquad (7)$$

where ρ_i, V_i, p_i are respectively the density, the volume and the pressure of the $i-$particle while $\boldsymbol{r}_i$ and $\boldsymbol{u}_i$ are its position and velocity. Here, W_{ij} is a weight function (also known as kernel function) which accounts for the interactions with the neighbor particles. The kernel function depends on $\|\boldsymbol{r}_j - \boldsymbol{r}_i\|$ and has a compact support which automatically defines the set $\mathscr{N}_i$. The radius of the compact support is proportional to a reference length, h, which is called smoothing length. Specifically, we choose a Wendland kernel with a support radius equal to $2\,h = 4\,\Delta x$. The symbol ∇_i denotes the differentiation with respect to $\boldsymbol{r}_i$ and $\boldsymbol{f}_i$ is the body force at the position $\boldsymbol{r}_i$. Finally, symbols ρ_0 and c_0 indicate the reference density and sound velocity (assumed to be constant). For computational reason, it is common practice in the weakly-compressible SPH solvers not to use the physical sound velocity but, conversely, to impose c_0 to be at least one order of magnitude greater than the maximum flow velocity, that is, $c_0 \geq 10 \max_i \|\boldsymbol{u}_i\|$. This assumption ensures the density variation to remain below 1%.

The viscous effects are modeled through the formulation proposed by Monaghan and Gingold [10]. The dynamic viscosity is denoted through μ while the kinematic viscosity is $\nu = \mu/\rho_0$. The argument of the viscous term is:

$$\pi_{ij} = K\, \frac{(\boldsymbol{u}_j - \boldsymbol{u}_i) \cdot (\boldsymbol{r}_j - \boldsymbol{r}_i)}{\|\boldsymbol{r}_j - \boldsymbol{r}_i\|^2}\,, \qquad (8)$$

where $K = 2\,(n + 2)$ and n is the number of spatial dimensions. Under the assumption that the fluid is incompressible, this term approximates the Laplacian of the velocity field (see, for example, [11]). For what concerns the time step, this is chosen as the minimum over three different reference times which represent the viscous, the advective and the acoustic time scales. These are respectively:
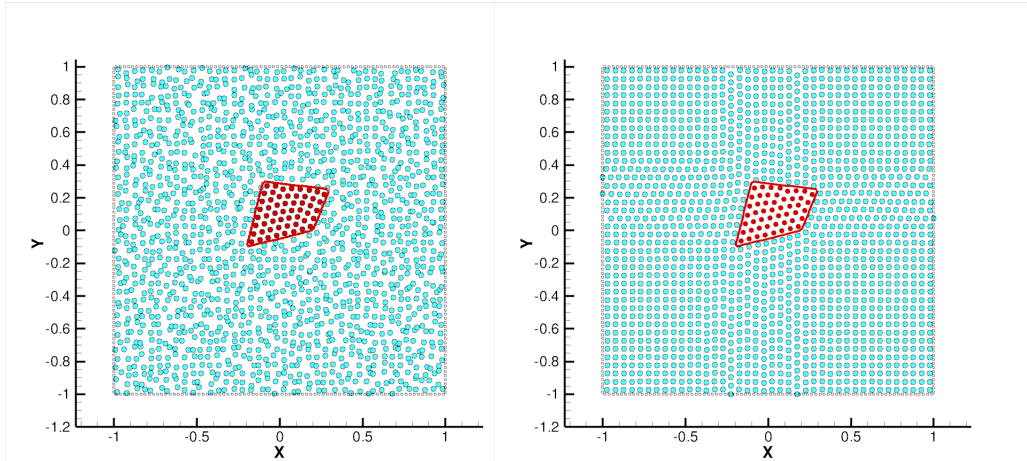
Fig. 6. The Packing Algorithm applied to a periodic fluid domain with an inner irregular body ($L/\Delta x = 40$). Left: initial configuration. Right: packed configuration.

$$\Delta t_1 = 0.125 \, \frac{h^2}{\nu} \,, \qquad \Delta t_2 = 0.25 \, \min_i \sqrt{\frac{h}{\|\boldsymbol{a}_i\|}} \,,$$

$$\Delta t_3 = 2.2 \, \min_i \left(\frac{h}{c_0 + \|\boldsymbol{u}_i\| + h \max_j |\pi_{ij}|} \right) \,, \tag{9}$$

where $\boldsymbol{a}_i$ is the particle acceleration.

3.1   The Packing Algorithm

In the present section we use the Λ-measure to study the behavior of an algorithm specifically conceived to initialize the particle positions for SPH simulations, i.e. the Particle Packing Algorithm proposed in [15]. In fact, a generic initial particle configuration usually induces some errors in the SPH pressure gradient operator. Specifically, this operator is not null even when the pressure field is constant. Such an issue leads to the generation of an initial particle resettlement and spurious noise which affect both the velocity and the pressure field. The Packing Algorithm displaces the fluid particle in order to minimize such an error and gives an initial configuration which is optimal for the SPH simulations. Generally, the configuration obtained after the use of the packing algorithm is very regular and homogeneous. The model equations of the Packing Algorithm are obtained from the SPH equations by assuming a constant pressure field and dropping the continuity equations (see [15] for more details).

To show the behavior of the packing algorithm and its relations with the particle disorder measure, we consider two test cases: a squared fluid domain with periodic boundaries of length L and the same domain with an inner
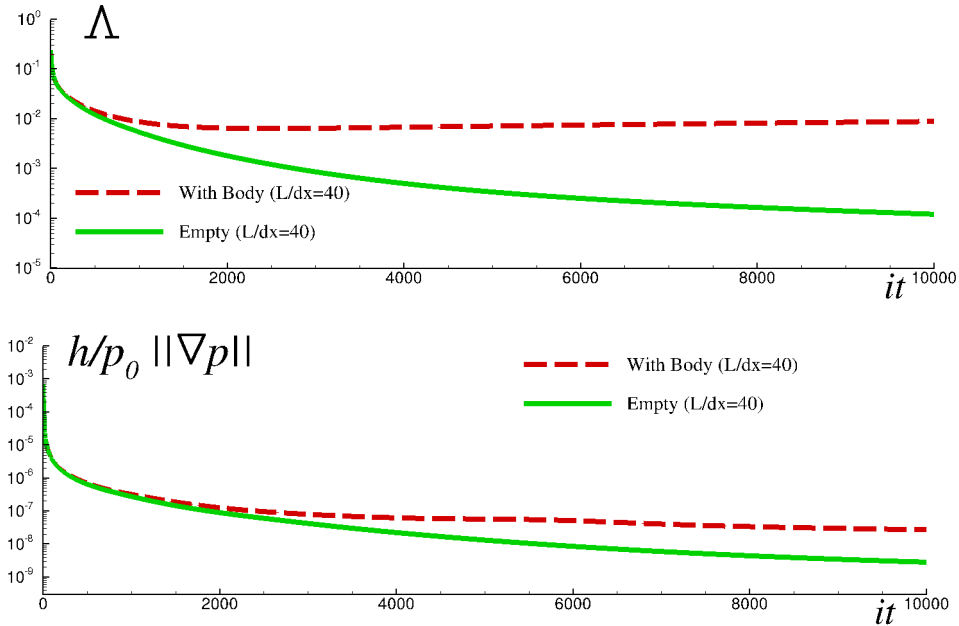
10

Fig. 7. The Packing Algorithm with and without the solid body for $L/\Delta x = 40$. Top panel: evolution of Λ. Bottom panel: error on the pressure gradient. Here, p_0 is the reference pressure field and h is the reference length for the kernel support(also known as smoothing length). The ordinate axis shows the number of iterations of the Packing Algorithm.

irregular solid body (see figure 6). In both the cases, the particles are initially set on a Cartesian grid perturbed by a random noise ($\epsilon_r = 0.25$, see Section 2.1) and the packing algorithm is used to attain a stable configuration. As expected, in the first case we obtain a regular configuration (specifically, we obtain back a Cartesian grid). Conversely, the presence of the solid body leads to a final configuration which is not perfectly regular (see the right panel of figure 6) even if it is characterized by a small value of Λ. This is shown in figure 7 where the evolution of Λ is displayed along with the L_2-error on the pressure gradient operator. In both the cases the error rapidly converges to zero, ensuring that the final particle configuration is stable (that is, it is not affected by a further particle resettlement). Conversely, the evolution of disorder measure is quite different. In fact, the presence of the solid body implies that Λ does not converge to zero, even though its asymptotic value is quite small ($\Lambda \simeq 10^{-2}$). This is an important point since it means that the SPH admits stable particle configurations even though such configurations are not perfectly regular.

3.2 *Disorder and SPH Interpolation*

Before proceeding to the analysis, it is interesting to draw some connections between the particle disorder and the SPH interpolation.

11

All SPH schemes rely on a smoothing procedure that, at the continuum, allows for a representation of functions and/or differential operators through convolutions integrals. Specifically, the differential operators are moved from the physical variables to the kernel function W_{ij} through integration by parts. At the discrete level, the convolution integrals are represented by convolution series, as done, for example, for the velocity divergence in the continuity equation of system (7).

The accuracy of the smoothing procedure depends on the particle distribution and may dramatically degrade as the particle disorder increases (see, for example, [5,12–14]). Quinlan et al. [5] were the first to obtain analytical estimates of the smoothing errors as function of the particle disorder. Unfortunately, their analysis mainly apply to one-dimensional problems, since in two and three dimensions it was not clear how the compact support of W_{ij} could be partitioned into analytically convenient sub-volumes assigned to each particle. In this context, the disorder measure can be profitably used to link the particle disorder to the accuracy of the smoothing procedure, disregarding the number of spatial dimensions. In the following part, we give a brief example of a possible application.
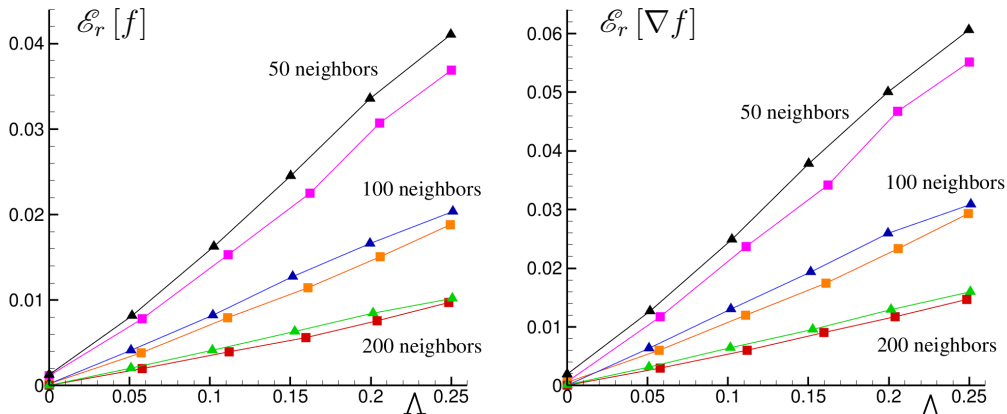

Fig. 8. Relative errors in the smoothing procedure for Cartesian (squared symbols) and Triangular grids (triangular symbols). Left: smoothing of a linear function. Right: SPH gradient of a linear function.

Let us consider a linear function in the (x, y)-plane, namely $f = 3\,x + 2\,y$, and define:

$$\langle f \rangle_i = \sum_j f_j\,W_{ij}\,V_j\,, \qquad \langle \nabla f \rangle_i = \sum_j (f_j - f_i)\,\nabla_i W_{ij}\,V_j\,. \tag{10}$$

Similarly to section 2.1, we consider a regular lattice (Cartesian and Triangular) perturbed by a Gaussian noise ($\epsilon_r = 0, 0.05, 0.1, 0.15, 0.2, 0.25$). The volumes V_j are assumed to be constant, since we observed that their variation according to the lattice perturbation only leads to negligible
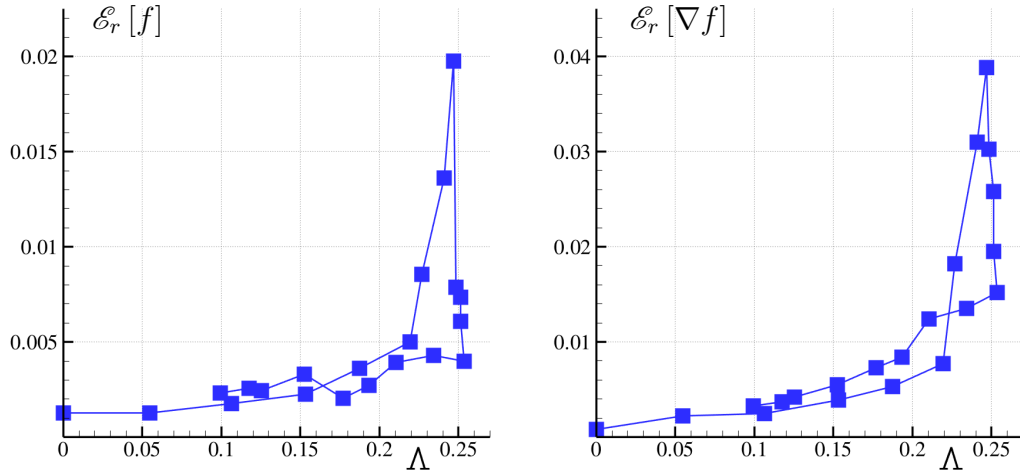
Fig. 9. Relative errors in the smoothing procedure of a linear field (left) and of its gradient (right). The particle distributions have been extracted from the evolution of the Taylor-Green vortex described in Section 3.3 ($L/\Delta x = 50$ and 50 neighbour particles). Lines connects points at subsequent instants of the evolution.

corrections to the values of $\langle f \rangle_i$ and $\langle \nabla f \rangle_i$. Finally, we compute the relative errors with respect to the analytic solutions, that is:

$$\mathscr{E}_r\left[f\right] = \frac{\sum_i |\langle f \rangle_i - f_i|}{\sum_i |f_i|}, \qquad \mathscr{E}_r\left[\nabla f\right] = \frac{\sum_i \|\langle \nabla f \rangle_i - \nabla f_i\|}{\sum_i \|\nabla f_i\|}. \qquad (11)$$

Figure 8 displays the behaviour of the relative errors as functions of Λ by varying the number of neighbours. Remarkably, in all the cases the errors depend almost linearly on the disorder measure, this confirming a strong correlation between such quantities.

Apart from this, it is interesting to repeat the above analysis with particle distributions obtained directly from SPH simulations. In effect, these are not completely random but depend on the fluid dynamics (i.e., on the specific problem at hand) and on a self-ordering mechanisms that acts during the evolution. Such a mechanism is similar to that at the basis of the packing algorithm ([15] and Section 3.1) and tends to rearrange particles in order to minimize the errors in the pressure gradient (see, for example, [16]). Despite this, the resulting particle distribution not always corresponds to a minimization of the particle disorder (this has been shown, for example, in the upper panel of figure 7).

To better describe such a phenomenon, we interpolated the linear field and its gradient on the SPH distributions obtained during the evolution of the Taylor-Green vortex described in Section 3.3. At the initial instant, the fluid particles are positioned on a regular Cartesian lattice. Figure 9 displays the relative errors by using a Wendland kernel with 50 neighbour particles. The

lines connects together points at subsequent instants of the evolution.

During the initial and final stages of the evolution, the disorder measure maintains small (i.e., $\Lambda \leq 0.15$) while the interpolation errors are much smaller than those shown in figure 8 for the Gaussian noise. Specifically, they maintain below 1% for both the linear field and its gradient. This behaviour suggests that the SPH succeeds in rearranging particles and minimizing the smoothing errors. Note that the interpolation errors increase almost linearly with Λ.

This behaviour drastically changes when the disorder exceeds a certain threshold values ($\Lambda > 0.2$ in figure 9). In this case, the SPH self-ordering mechanism proves to be ineffective and the interpolation errors suddenly increase up to values that are comparable with those displayed for the Gaussian noise (see figure 8). In such a range we may find configurations characterized by similar values of Λ but with very different interpolation errors. These variations discriminate the cases where the SPH self-ordering mechanism succeeds or not.

Then, in practical simulations it is not always possible to draw a strong correlation between the disorder measure and the interpolation errors like that displayed for the random Gaussian noise. In any case, small values of Λ (e.g. $\Lambda < 0.15$) seem to guarantee the accuracy of the SPH discrete operators.

3.3 Taylor-Green vortex

In the present section we consider the Taylor-Green vortex (the analytic solution may be found in [17]). Specifically, we consider a patch of four vortexes (see the top left panel of figure 10) with Reynolds number $Re = 2\pi LU/\nu = 400$ (here L is the reference length and U is the maximum initial velocity).

Figure 10 shows some sketches of the evolution of the vorticity field (left panels) and of the local measure λ_i. The fluid particles are initially positioned on a Cartesian grid and λ_i is zero everywhere as required. During the evolution, because of the Lagrangian nature of the SPH, the fluid particles tend to clump along the stream lines, leading to large values of λ_i (see the middle panels of figure 10). As we shall discuss later in the paper, such an anisotropic particle configuration may lead to large errors in the numerical solution (see, for example, [5,8,18,19]). In any case, for longer times the particles resettle on a more regular configuration (bottom middle panels of figure 10) and, finally, the vortexes are damped by the action of the fluid viscosity. During these stages, the values of the local measure decrease and the particle distribution becomes more and more regular.

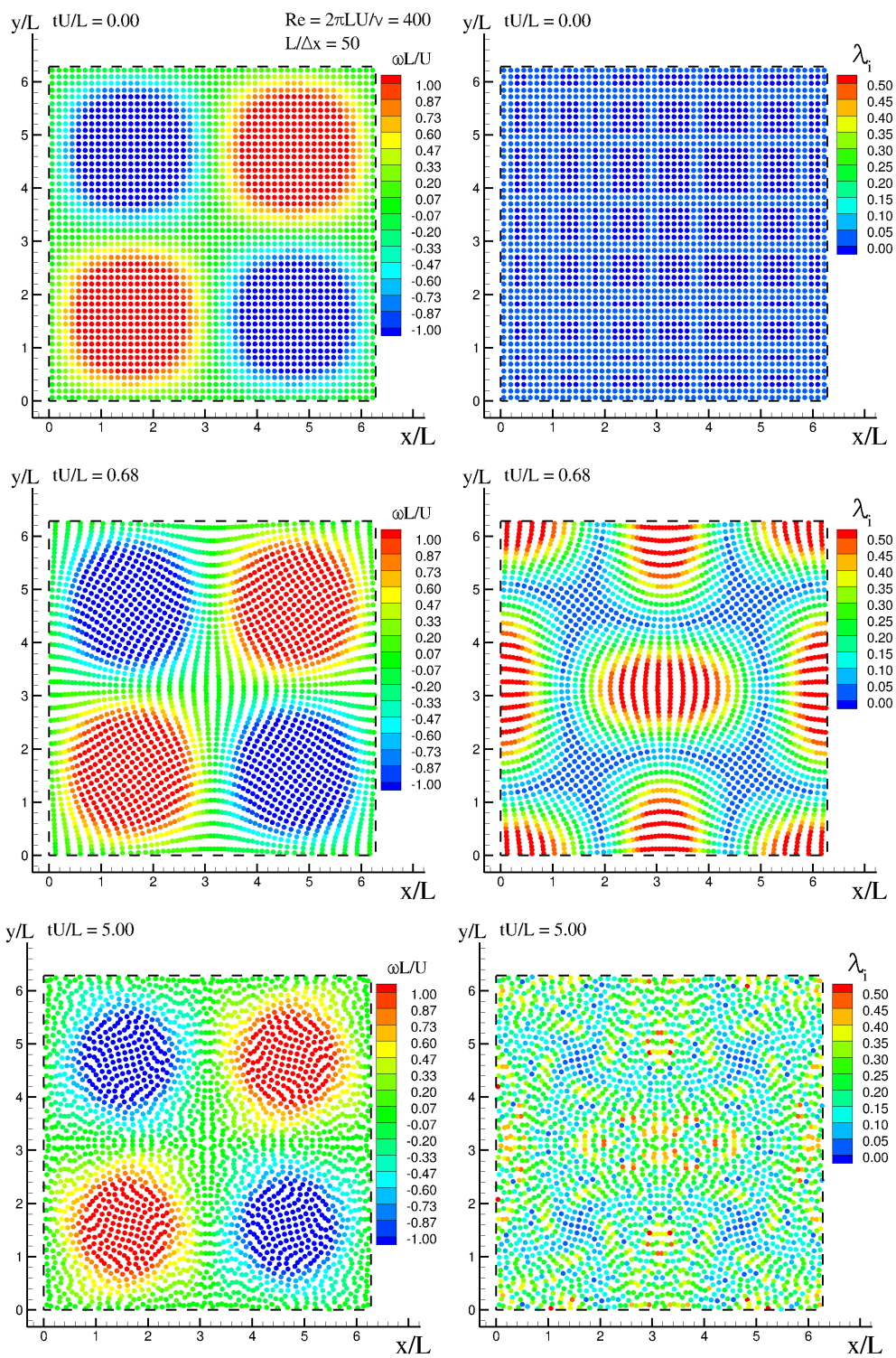Figure 11 displays the evolution of the global measure Λ for increasing spatial

Fig. 10. The Taylor-Green vortices. Right plots: evolution of the vorticity field. Left plots: evolution of the *local* measure λ_i.
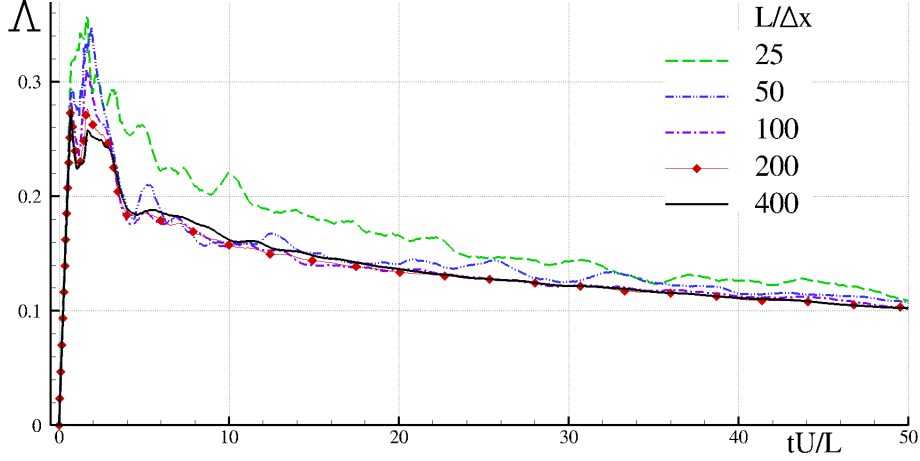
Fig. 11. The Taylor-Green vortexes. Evolution of Λ for increasing spatial resolutions.
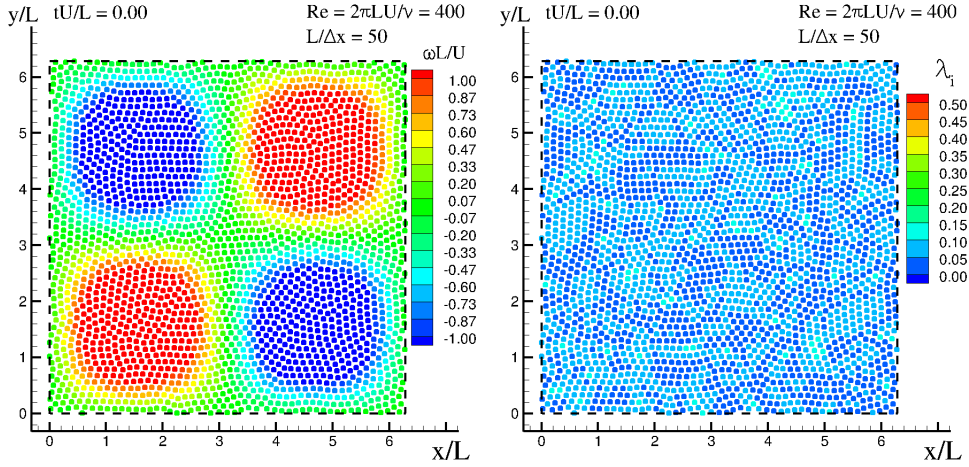

Fig. 12. The Taylor-Green vortexes initialized by using the particle packing algorithm described in [15]. Left panel: the vorticity field. Right panel: the local measure λ_i.

resolutions. The initial peaks correspond to the maximum particle clumping along the stream lines while the subsequent decrease is associated with the particle resettlement. It is interesting to note that the SPH is converging to the analytic solution (this is shown in the final part of the present section) but the measure Λ is not decreasing any more. In any case, Λ approaches a converged solution as well. Further, for long times Λ tends to an asymptotic value which is sensibly different from zero (i.e. $\Lambda \simeq 0.1$). At this stage the fluid is practically motionless. This means that a converged and stationary SPH simulation does not necessarily display a perfectly uniform particle distribution, even though the global and local disorder is generally very small. This behavior has been already observed by Monaghan [2] and by Lind et al.[8].

In the last part of the analysis, we repeat the simulation with $L/\Delta x = 50$ by using the particle packing algorithm to initialize the particle positions. The initial instant is displayed in figure 12. In this case, the λ_i-field is not perfectly
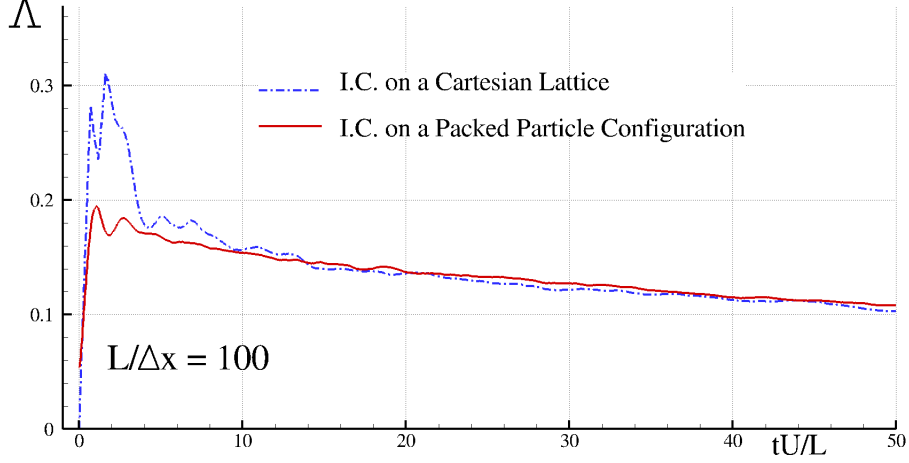
16

Fig. 13. The Taylor-Green vortexes. Evolution of Λ with and without the use of the particle packing algorithm.
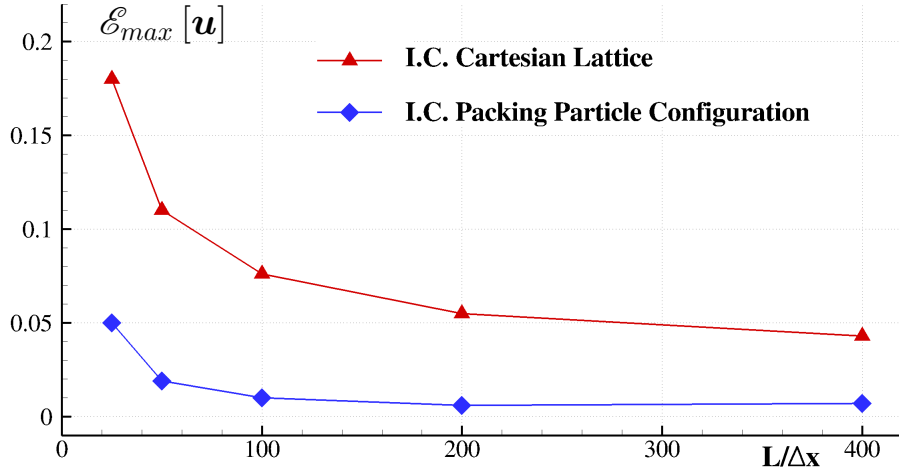

Fig. 14. The Taylor-Green vortexes. The maximum global error on the velocity field with and without the use of the particle packing algorithm.

zero even though its variations are smaller than 0.1. The evolution of the global measure is shown in figure 13. Since the use of the packing algorithm eliminates the particle resettlement, the initial peak of Λ disappears. Apart from this, the long-time evolution of the two cases is almost identical even if the accuracy of the simulation increases when the packing algorithm is adopted. This is briefly displayed in figure 14 where the maximum global error on the velocity field is shown for different resolutions. Specifically, we consider:

$$\mathscr{E}_{max}\left[\boldsymbol{u}\right] \;=\; \max_{t}\|\boldsymbol{u} - \boldsymbol{u}_{an}\|_1/U_{max} \tag{12}$$

where $\boldsymbol{u}_{an}$ is the analytic solution, $\|\cdot\|_1$ is the L_1-norm and U_{max} is the (analytic) maximum velocity at the initial time.
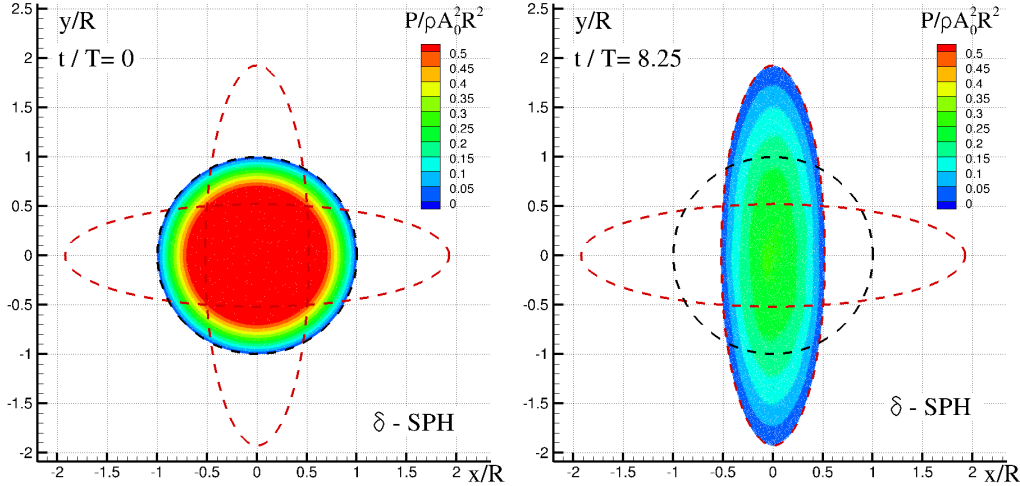
17

Fig. 15. Oscillating drop. Initial (right plot) and final instant (left plot) of the evolution. The dashed lines indicate the analytic solution of the free surface ($R/\Delta x = 100$).

3.4   Oscillating drop under a central conservative force field

In the present section we consider a two-dimensional fluid drop evolving under the action of a central conservative force field, $-B^2\, \boldsymbol{r}$, where B is a dimensional parameter. The fluid is inviscid (i.e. $\mu = 0$) and the drop is initially circular with radius R. The drop evolves periodically as an oscillating fluid ellipse, according to the following law:

$$
\begin{cases}
u = A(t)\, x \\
v = -A(t)\, y\,,
\end{cases}
\tag{13}
$$

where the solution for $A(t)$ is given in [20]. It is simple to show that the global dynamics depends on the ratio $A(0)/B$, which, in the following simulations, is set equal to 1.

The present test case is used to show a further interesting application of the disorder measure: we inspect how different formulations of the same numerical scheme may lead to different particle distributions. In this specific case, the standard SPH scheme described in section §3 is compared with a diffusive variant, namely the δ-SPH scheme. This scheme contains a diffusive term inside the continuity equation which helps to reduce the spurious high-frequency noise which generally affects the pressure field. More details may be found in Antuono et al. [21].

Figure 15 displays the initial and the final instant of the evolution obtained by using the δ-SPH scheme and the analytic solution of the free surface (dashed
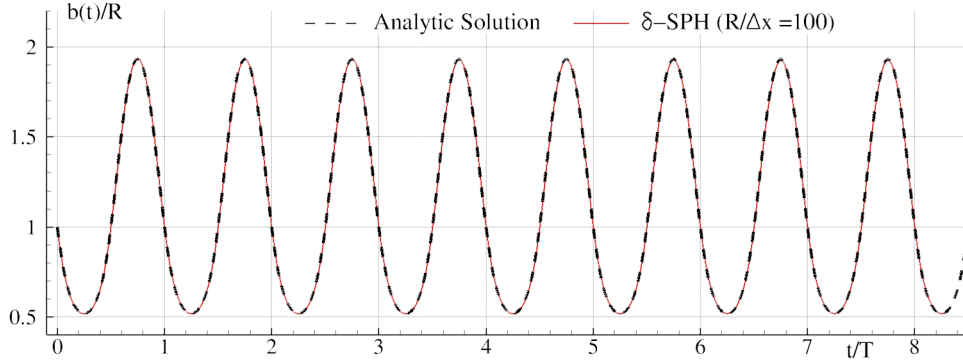
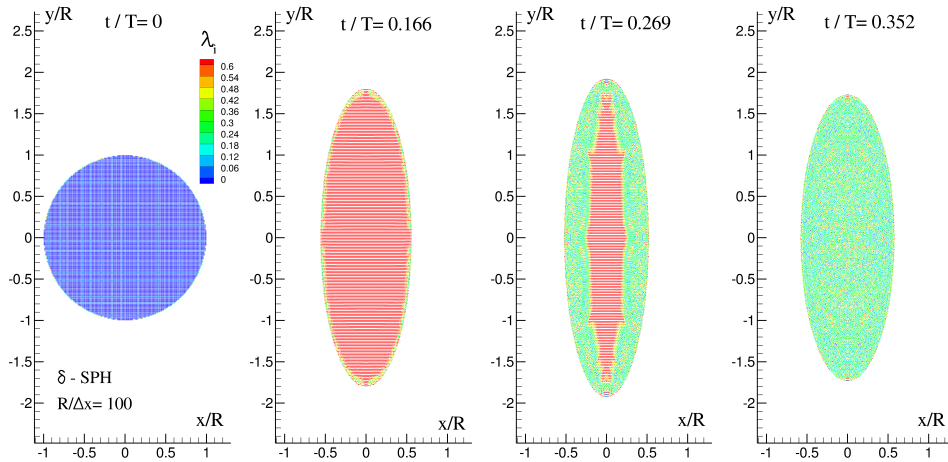Fig. 16. Oscillating drop. Comparison with the analytic solution for the ellipse semi-axis, $b(t)$.

Fig. 17. Oscillating drop. The local measure λ_i during the early stages of the evolution ($R/\Delta x = 100$).

lines). The overall comparison is very good and it is further confirmed in figure 16, where the δ-SPH solution is compared with the analytic solution for the ellipse semi-axis, $b(t)$. No spurious numerical damping is observed, this confirming the reliability of the δ-SPH for inviscid problems, at least in a limited time range. Despite this, the particle disorder is small but not negligible (see figure 17 and the left plot of figure 18). This is consistent with the results observed in sections 3.1 and 3.3: the convergence of the considered SPH schemes does not imply that the particle distribution is perfectly regular. It seems that, below a certain value of Λ, the particle disorder plays a minor role and the considered SPH schemes compensate somehow the interpolation errors. This is an important issue and will be the subject of future inspections.

The evolution of the local measure is displayed in figure 17. Since at the initial instant the particles are on a Cartesian grid, λ_i is identically null inside the fluid bulk and it is slightly larger than zero just along the free surface because of the local nonuniform distribution. Then, due to the drop stretching, the distance among the particle rows increases and λ_i increases as well (see the second panel of figure 17). At a certain moment, the particles close to the free
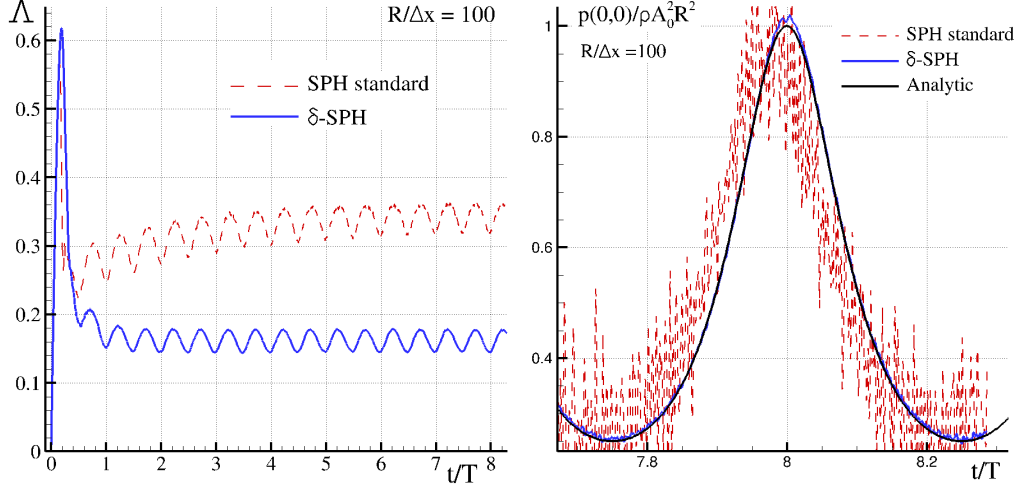
19

Fig. 18. Oscillating drop. The evolution of Λ (left plot) and of the pressure at the origin (right plot) for the standard and δ-SPH.
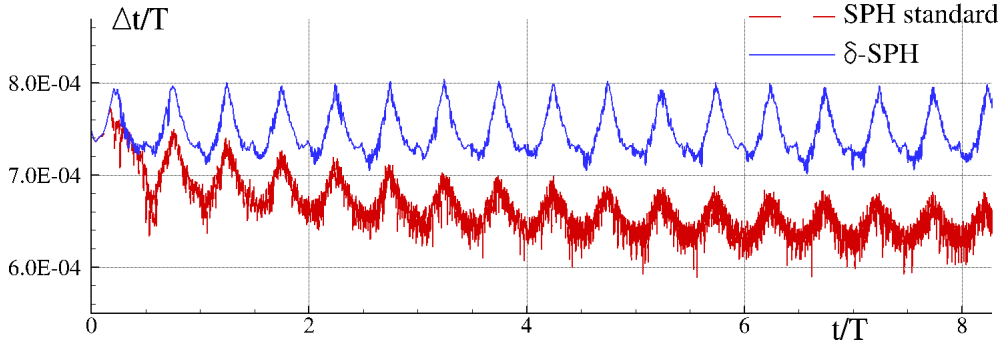

Fig. 19. Oscillating drop. Comparison between the time stepping of the δ-SPH and of the standard SPH

surface start resettling and such a resettlement rapidly propagates all over the fluid domain (third and fourth panel of figure 17). This phenomenon has been described in [16] and corresponds to a drastic reduction of the particle disorder and to a consequent decrease of λ_i.

The evolution of the global measure Λ is shown in the left plot of figure 18. Apart from the initial instants (which are clearly dominated by the particle stretching and resettlement), the comparison between the δ-SPH and the standard SPH clearly proves that the former one is characterized by a more regular particle distribution. This has a crucial influence on the accuracy of the simulation, as shown in the right plot of figure 18 where the time history of the pressure at the origin is displayed for both the SPH schemes. Here, the standard SPH scheme is affected by a spurious high-frequency noise while the δ-SPH scheme provides a smooth pressure profile and a good agreement with the analytic solution. Through the formulae in equation (9), the increased regularity and accuracy of the numerical solution also reflects on a larger time stepping of the δ-SPH in comparison to the standard SPH (see figure 19).
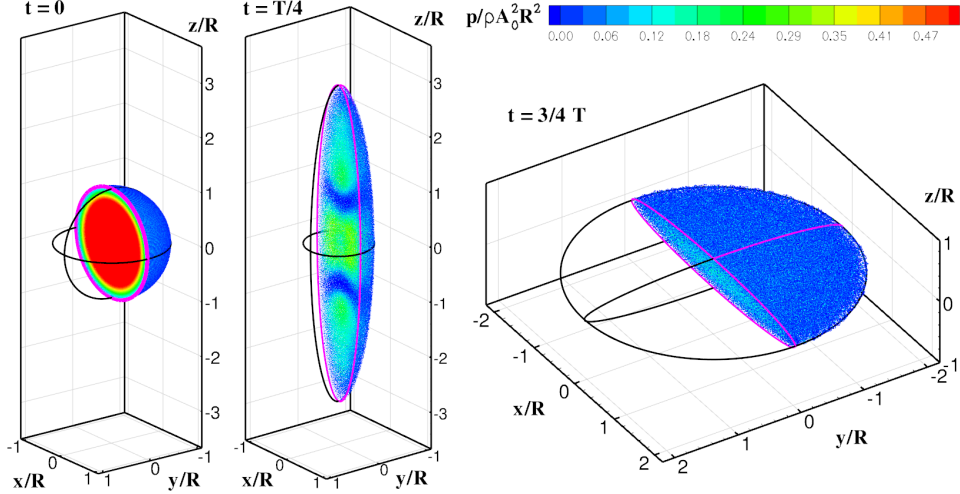
20

Fig. 20. three-dimensional oscillating drop. Sketches of the evolution and contour zones of the pressure field $(R/\Delta x = 50)$. The solid lines represent specific sections of the analytic free surface.

3.4.1 Extension to three dimensions

The two-dimensional solution provided in the previous section can be easily extended in three dimensions. In this case the drop evolves like a spheroid, according to the following law:

$$
\begin{cases}
u = -A(t)\,x \\
v = -A(t)\,y \\
w = 2\,A(t)\,z\,,
\end{cases}
\tag{14}
$$

and the solution for $A(t)$ is given in [20], as well. Similarly to the two-dimensional case, the global dynamics depends on the ratio $A(0)/B$ (where B is the coefficient of the central conservative force field). In the following simulations, this ratio is set equal to 1.

Figure 20 shows some snapshots of the evolution along with the contour zones of the pressure field obtained by using the δ-SPH scheme. For graphical reasons, only half of the fluid domain is displayed while the solid lines represent specific sections of the analytic free surface. The circular drop initially stretches along the vertical direction in form of a prolate spheroid (left panel of figure 20), reaches the maximum elongation (central panel) and, then, shrinks to form an oblate spheroid (right panel of the same figure). In all the cases, the numerical solution is in a good agreement with the analytic solution for the free surface.

The procedure used to build the disorder measure Λ can be straightforwardly
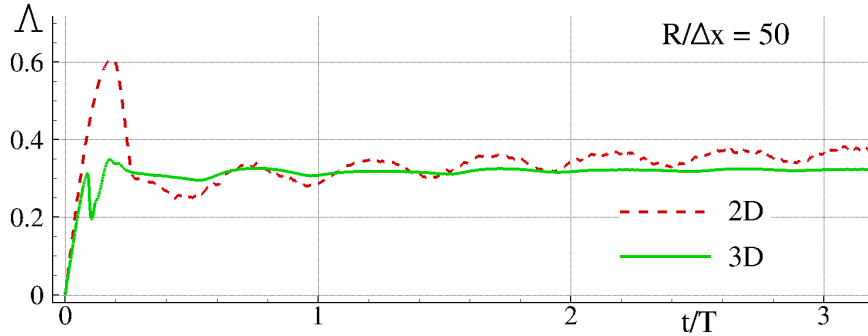
21

Fig. 21. three-dimensional oscillating drop. Evolution of the measure Λ and comparison with the two-dimensional problem.

applied to the three dimensional problem. In this case it is interesting to compare the evolution of Λ with the two dimensional simulation (see figure 21). In three dimensions the time history of Λ does not exhibit the initial peak since the particle resettlement is weaker. Intuitively, this is due to the fact that in three dimensions particles have more degrees of freedom and, consequently, they rearrange previously than the two dimensional case and with weaker dynamics. Apart from this, the long time evolution is similar in both the cases.

Conclusions

Based only on geometrical considerations, we proposed an algorithm to measure the disorder in a generic particle distribution. The proposed measure applies to both two- and three-dimensional problems and can be qualitatively regarded as the mean absolute value of the perturbation with respect to a hypothetical regular lattice.

Possible practical applications of the proposed disorder measure have been provided by using the Smoothed Particle Hydrodynamics scheme and considering both two- and three-dimensional simulations. The numerical simulations highlighted how Λ can be used to inspect the relation between the particle disorder and the accuracy of the numerical scheme and to compare different variants of the same numerical method. The proposed measure may be also adopted to monitor the particle disorder during simulations and decide when/if re-meshing or packing algorithms have to be used. This would help to optimize the implementation of such tools, reducing the computational costs.

In all the considered cases, the disorder measure proved to be reliable and to qualitatively discriminates between more and less regular particle distributions.

22

A   Random noise on a regular lattice

Let us consider a regular grid with uniform spacing Δx and two independent random variables, say x and y, with the same density distribution and with zero mean, that is $\mathbb{E}(x) = \mathbb{E}(y) = 0$. Starting from them, we derive two new independent variables, namely X and Y, with the same probability distribution of x and y, with zero mean and which satisfy:

$$\mathbb{E}(Z) = \mathbb{E}\left(\sqrt{X^2 + Y^2}\right) = \epsilon_r \, \Delta x \, . \tag{A.1}$$

Here ϵ_r is assigned and represents the mean absolute relative error with respect to the regular grid. The variables X and Y are used to perturb the horizontal and vertical coordinates of the grid points of the regular lattice.

The derivation of X and Y is straightforward. We introduce a positive parameter α and set $X = \alpha \, x$ and $Y = \alpha \, y$. By definition, X and Y have the same probability distribution of x and y, are independent and have zero mean. The parameter α is obtained by satisfying the requirement in (A.1):

$$\mathbb{E}(Z) = \alpha \, \mathbb{E}\left(\sqrt{x^2 + y^2}\right) = \epsilon_r \, \Delta x \qquad \Rightarrow \qquad \alpha = \frac{\epsilon_r \, \Delta x}{\mathbb{E}\left(\sqrt{x^2 + y^2}\right)} \, .$$

It is simple to show that the variance of the new variables is $\mathbb{V}(X) = \alpha^2 \, \mathbb{V}(x)$ and $\mathbb{V}(Y) = \alpha^2 \, \mathbb{V}(y)$. Then, the larger the relative error ϵ_r, the larger the variance. In our computations we use a Normal Gaussian distribution and a Uniform distribution in $[0, 1]$ for x and y.

References

[1] S. R. Idelsohn, E. Oñate, F. Del Pin. *The particle finite element method: a powerful tool to solve incompressible flows with free-surfaces and breaking waves*, International Journal for Numerical Methods in Engineering, **61**: 964-989 (2004).

[2] J.J. Monaghan, *Smoothed Particle Hydrodynamics*, Rep. Prog. Phys. **68**, 1703–1759, (2005).

[3] G. H. Cottet & P. D. Koumoutsakos, *Vortex Methods: Theory and Practice*, Cambridge University Press, March 13-th, 2000

[4] P. D. Koumoutsakos, *Multiscale Flow Simulations using Particles*, Annu. Rev. Fluid Mech. **37**: 457-487, 2005.

[5] N. J. Quinlan, M. Basa, M. Lastiwka, *Truncation error in mesh-free particle methods*, Int. J. Numer. Meth. Engng., **66**: 2064-2085 (2006)

[6] A. K. Chaniotis, D. Poulikakos, P. Koumoutsakos, *Remeshed Smoothed Particle Hydrodynamics for the Simulation of Viscous and Heat Conducting Flows*, Journal of Computational Physics, **182**(1): 67-90, 2002.

[7] S. Børve, M. Omanq, J. Trulsen, *Regularized smoothed particle hydrodynamics: a new approach to simulating magneto-hydrodynamic shocks*, Astrophys. J., **561**, 82-93, (2001)

[8] S. J. Lind, R. Xu, P. K. Stansby, B. D. Rogers, *Incompressible smoothed particle hydrodynamics for free-surface flows: A generalised diffusion-based algorithm for stability and validations for impulsive flows and propagating waves*, J. Comput. Phys., **231**(4), 1499-1523, (2012)

[9] R. Vacondio, B. D. Rogers, P. K. Stansby, *Smoothed Particle Hydrodynamics: Approximate zero-consistent 2-D boundary conditions and still shallow-water tests*, Int. J. Num. Meth. Fluids, **69**(1), 226-253, (2012)

[10] J. J. Monaghan and R. A. Gingold, *Shock simulation by the particle method SPH*, J. Comput. Phys., **52**(2), 374-389, (1983)

[11] A. Colagrossi, M. Antuono, A. Souto-Iglesias, D. Le Touzé, David, *Theoretical analysis and numerical verification of the consistency of viscous smoothed-particle-hydrodynamics formulations in simulating free-surface flows*, Physical Review E, **84**(2), 026705, (2011)

[12] A. Colagrossi, *A meshless lagrangian method for free-surface and interface flows with fragmentation*, PhD Thesis, Università degli Studi di Roma "La Sapienza", 2005

[13] A. Amicarelli, J-C. Marongiu, F. Leboeuf, J. Leduc, M. Neuhauser, L. Fang, J. Caro, *SPH truncation error in estimating a 3D derivative*, International Journal for Numerical Methods in Engineering, **87**(7), 677-700, (2011)

[14] A. Amicarelli, J-C. Marongiu, F. Leboeuf, J. Leduc, J. Caro, *SPH truncation error in estimating a 3D function*, Computers & Fluids , **44**(1), 279-296, (2011)

[15] A. Colagrossi, B. Bouscasse, M. Antuono, S. Marrone, *Particle packing algorithm for SPH schemes*, Computer Physics Communications, **183**, 1641-1653, (2012)

[16] D. Le Touzé, A. Colagrossi, G. Colicchio, M. Greco, *A critical investigation of Smoothed Particle Hydrodynamics applied to problems with free surfaces*, International Journal of Numerical Methods in Fluids, **73**, 660-691, (2013)

24

[17] G. I. Taylor and A. E. Green, *Mechanism of the Production of Small Eddies from Large Ones*, Proc. R. Soc. Lond. A, **158**, 499-521 (1937).

[18] R. Xu, P. K. Stansby, D. Laurence, *Accuracy and stability in incompressible SPH (ISPH) based on the projection method and a new approach*, J. Comput. Phys., **228**(18), 6703-6725, (2009)

[19] R. Vacondio, B. D. Rogers, P. K. Stansby, P. Mignosa, *A correction for balancing discontinuous bed slopes in two-dimensional smoothed particle hydrodynamics shallow water modeling*, Int. J. Num. Meth. Fluids, **71**(7), 850-872, (2013)

[20] J. J. Monaghan and Ashkan Rafiee, *A simple SPH algorithm for multi-fluid flow with high density ratios*, Int. J. Numer. Meth. Fluids, **71**: 537-561 (2013)

[21] M. Antuono, A. Colagrossi, S. Marrone, *Numerical diffusive terms in weakly-compressible SPH schemes*, Computer Physics Communications **183**: 2570-2580 (2012)